A&A 530, A110 (2011)
DOI: 10.1051/0004-6361/201116876

Astronomy & Astrophysics

Exploring the galaxy cluster-group transition regime at high redshifts

Physical properties of two newly detected $z > 1$ systems⋆

R. Šuhada[1], R. Fassbender[1], A. Nastasi[1], H. Böhringer[1], A. de Hoon[2], D. Pierini⋆⋆, J. S. Santos[3], P. Rosati[4], M. Mühlegger[1], H. Quintana[5], A. D. Schwope[2], G. Lamer[2], J. Kohnert[2], and G. W. Pratt[6]

[1] Max-Planck-Institut für extraterrestrische Physik (MPE), Giessenbachstrasse 1, 85748 Garching, Germany
e-mail: rsuhada@mpe.mpg.de
[2] Astrophysikalisches Institut Potsdam (AIP), An der Sternwarte 16, 14482 Potsdam, Germany
[3] European Space Astronomy Centre (ESAC)/ESA, Madrid, Spain
[4] European Southern Observatory (ESO), Karl-Schwarzschild-Str. 2, 85748 Garching, Germany
[5] Departamento de Astronomía y Astrofísica, Pontificia Universidad Católica de Chile, Casilla 306, Santiago 22, Chile
[6] CEA Saclay, Service d'Astrophysique, L'Orme des Merisiers, Bât. 709, 91191 Gif-sur-Yvette Cedex, France

Received 12 March 2011 / Accepted 13 April 2011

ABSTRACT

Context. Multi-wavelength surveys for clusters of galaxies are opening a window on the elusive high-redshift ($z > 1$) cluster population. Well controlled statistical samples of distant clusters will enable us to answer questions about their cosmological context, early assembly phases and the thermodynamical evolution of the intracluster medium.
Aims. We report on the detection of two $z > 1$ systems, XMMU J0302.2-0001 and XMMU J1532.2-0836, as part of the *XMM-Newton* Distant Cluster Project (XDCP) sample. We investigate the nature of the sources, measure their spectroscopic redshift and determine their basic physical parameters.
Methods. The results of the present paper are based on the analysis of *XMM-Newton* archival data, optical/near-infrared imaging and deep optical follow-up spectroscopy of the clusters.
Results. We confirm the X-ray source XMMU J0302.2-0001 as a gravitationally bound, bona fide cluster of galaxies at spectroscopic redshift $z = 1.185$. We estimate its M_{500} mass to $(1.6 \pm 0.3) \times 10^{14}\ M_{\odot}$ from its measured X-ray luminosity. This ranks the cluster among intermediate mass system. In the case of XMMU J1532.2-0836 we find the X-ray detection to be coincident with a dynamically bound system of galaxies at $z = 1.358$. Optical spectroscopy reveals the presence of a central active galactic nucleus, which can be a dominant source of the detected X-ray emission from this system. We provide upper limits of X-ray parameters for the system and discuss cluster identification challenges in the high-redshift low-mass cluster regime. A third, intermediate redshift ($z = 0.647$) cluster, XMMU J0302.1-0000, is serendipitously detected in the same field as XMMU J0302.2-0001. We provide its analysis as well.

Key words. galaxies: clusters: general – X-rays: galaxies: clusters – galaxies: evolution

1. Introduction

The number of known galaxy cluster detections at high redshift ($z \gtrsim 1$) is constantly growing (see Appendix B). Recently we have witnessed the detection of the first spectroscopically confirmed clusters at redshift >1.6 by Papovich et al. (2010) and Tanaka et al. (2010). This distance record has been however soon overtaken by the cluster XMMU J105324.7+572348 with $z = 1.753$ (Henry et al. 2010). Finally, Gobat et al. (2011) reported on the detection of a remarkable structure which is consistent with a low mass cluster at redshift 2.07. The nature of another potentially very distant system, JKCS041 detected by Andreon et al. (2009) at a photometric redshift of 1.9, was contested by Bielby et al. (2010). Recently obtained deep z' and J imaging, however seems to confirm the presence of a cluster at $z = 2.2$ (based on a red sequence redshift estimation).

For the first time we can start constructing sizable cluster samples at $z > 1$ as a consequence of several important factors. First, there is progress in cluster search methods, both classical such as X-ray (Mullis et al. 2005; Stanford et al. 2006; Henry et al. 2010; Fassbender et al. 2011a, Nastasi et al., in prep.) and optical/mid-infrared surveys (Gladders & Yee 2005; Stanford et al. 2005; Gobat et al. 2011; Papovich et al. 2010) as well as new selection methods like surveys utilising the Sunyaev-Zel'dovich effect (SZE, Planck Collaboration et al. 2011; Williamson et al. 2011; Vanderlinde et al. 2010; Marriage et al. 2011).

The second essential prerequisite is the availability of deep spectroscopic data, required to the confirm the cluster candidates as genuine gravitationally bound systems and to estimate their redshifts. This typically requires considerable effort and exposure times, and therefore many of the current crop of distant clusters are the results of observational campaigns spanning several years.

⋆ Based on observations obtained with ESO Telescopes at the Paranal Observatory under program ID 080.A-0659 and 081.A-0312, observations collected at the Centro Astrnómico Hispano Alemán (CAHA) at Calar Alto, Spain operated jointly by the Max-Planck Institut für Astronomie and the Instituto de Astrofísica de Andalucía (CSIC). X-ray observations were obtained by *XMM-Newton*.
⋆⋆ Visiting astronomer at MPE.

Table 1. Observation log of the X-ray coverage of XMMU J0302.2-0001 and XMMU J1532.2-0836.

Cluster	Instrument	OBSID	Exp. time (PN/MOS) [ks]	Off-axis angle
XMMU J0302.2-0001	XMM	0041170101	36.4/46.2	10.9′
XMMU J1532.2-0836	XMM	0100240701	13.2/17.4	5.0′
XMMU J1532.2-0836	XMM	0100240801	19.4/25.8[†]	6.1′

Notes. The quoted exposure times are net clean times. MOS1 and MOS2 exposure times are averaged. The off-axis angle for the *XMM-Newton* observations is an average angle from all three detectors. [(†)] This observation is heavily contaminated by quiescent proton flaring and used only for systematics check (Sects. 2.3 and 3.2).

In addition, at $z > 1.5$ we are also nearing to the edge of capabilities of even the largest optical spectroscopic instruments, since at these redshifts the 4000 Å-break (an important feature to anchor the redshift of passive galaxies) is redshifted beyond 10 000 Å, towards the tails of the sensitivity curves of current spectrographs. Fortunately, near-infrared spectroscopy is able to overcome this problem (e.g. Tanaka et al. 2010). Existing (e.g. MOIRCS on the Subaru telescope and LUCIFER at the Large Binocular Telescope) and upcoming (KMOS at the VLT) instruments will soon be able to provide confirmation for new high redshift clusters with a much higher efficiency than the optical spectrographs.

Even though studying high redshift systems is a truly daunting task, the effort is rewarded by gaining a direct view of the earliest assembly epochs of the most massive Dark Matter (DM) halos today, their gas content – the intracluster medium (ICM) – and their galaxy populations. Since the properties of the cluster population are intrinsically connected to the underlying cosmology, they provide a sensitive test of the cosmological parameters.

The high-mass end of the cluster mass function at high-redshift provides the best leverage when constraining cosmological parameters through their effect on the distribution and growth of the large scale structure. Since massive distant clusters are rare, this regime can be effectively probed only by surveys which are able to cover large sky areas (and hence large survey volumes) such as the SZE surveys. The selection function of these surveys is (almost) independent of redshifts and their sensitivity is limited to very massive clusters with minimal mass $3{-}5 \times 10^{14}\ M_{\odot}$ (Vanderlinde et al. 2010; Williamson et al. 2011; Marriage et al. 2011).

However, the majority of the cluster population lies below this mass threshold. Therefore, if we want to understand the thermodynamical evolution of the ICM and the evolution of the galaxy population, we have to look at lower mass systems down to the group regime. For the purpose of this paper we will consider the cluster-group transition regime to be around $\sim 1 \times 10^{14}\ M_{\odot}$. This threshold region can be probed by X-ray surveys, but it is at the very limit of feasibility of contemporary X-ray surveys (joint X-ray and near-infrared detections can reach slightly lower limiting masses, e.g. Finoguenov et al. 2010). Accessing this threshold population will, however, allow us to directly calibrate the mass scaling relations for less massive systems and study potential mass-dependent effects on the evolution of the galaxy population of the clusters.

Already a simple consideration from the virial theorem (Kaiser 1986) predicts a tight link between the ICM's properties (luminosity, temperature, gas mass) and the total mass (i.e. including DM). These quantities are thus not only of interest from the point of view of characterising the physical conditions of a given cluster, but also as an important observational input for cosmological studies. While the scaling relations of nearby clusters are fairly well known (e.g. Pratt et al. 2009; Arnaud et al. 2005), the evolution of these relations is only starting to be explored at redshifts $z \gtrsim 0.5{-}0.7$ (Vikhlinin et al. 2009; Pacaud et al. 2007). The $z > 1$ regime is still practically unexplored.

The redshift range $z = 1{-}2$ is a transition period also for the galaxy population of clusters. Local clusters exhibit typically well-defined red-sequences populated by passively evolving early-type galaxies. While similar red sequences are found also in some of the high redshift clusters, e.g. the very massive cluster XMMU J2235.3-2557 (Strazzullo et al. 2010; Rosati et al. 2009), we are finding more and more cases, where star-formation is still ongoing (Fassbender et al. 2011b; Hayashi et al. 2010; Hilton et al. 2010).

Sizable, well controlled cluster samples at high redshift are thus important to address many questions about the cluster population as a whole, but also about the underlying cosmology. In this paper we provide first details on two new, X-ray selected clusters at $z > 1$. In Sect. 2 we describe their detection and follow-up observations (imaging and spectroscopy). Optical properties are summarized in Sect. 2.2.1 and the X-ray analysis in Sect. 2.3. We discuss the results and draw conclusions in Sects. 3 and 4, respectively. The analysis of a third, intermediate redshift cluster ($z = 0.647$), serendipitously detected together with XMMU J0302.2-0001, is provided in Appendix A.

Throughout the article, we adopt a ΛCDM cosmology with $(\Omega_{\Lambda}, \Omega_{\rm M}, H_0, w) = (0.7, 0.3, 70\ {\rm km\ s^{-1}\ Mpc^{-1}}, -1)$. Physical parameters are estimated within an aperture corresponding to a factor 500 overdensity with respect to the *critical* density of the Universe at the cluster redshift. All quoted magnitudes are given in the AB system.

2. Observations and data analysis

The analysis of the presented clusters is based on archival, medium-deep X-ray observations and optical/near-infrared data (both imaging and spectroscopic) collected in a follow-up campaign. All the observations are summarized in Tables 1 and 2.

2.1. Initial X-ray detection with XMM-Newton

Both XMMU J0302.2-0001 and XMMU J1532.2-0836 were detected as extended X-ray sources in the framework of the *XMM-Newton* Distant Cluster Project (XDCP). The XDCP consists of 470 *XMM-Newton* archival fields with a total non-overlapping area close to 80 deg^2. The data was obtained from the XMM data archive[1]. The initial cluster detection was performed with the *XMM-Newton* science analysis system SAS v6.5 utilising a sliding box detection and a maximum likelihood source fitting[2]. Details of the source detection pipeline can be found in Fassbender (2008).

For the purposes of this paper we re-analyzed the observations containing both sources with the current updated version

[1] `xmm.esac.esa.int/xsa/`

[2] SAS tasks `eboxdetect` and `emldetect`.

Table 2. Summary of the optical/near-infrared observations of XMMU J0302.2-0001 and XMMU J1532.2-0836 analysed in this work.

Cluster	Data	Exposure time	Prog. ID	Date	Grism/Band	Seeing
XMMU J0302.2-0001	VLT/FORS2/ MXU spec.	3h (8×1308 s)	080.A-0659	2008 Jun. 6	300 I	$1.03''-1.26''$
XMMU J1532.2-0836	VLT/FORS2/ MXU spec.	3h (8×1308 s)	081.A-0312	2008 Apr. 4, 7	300 I	$0.79''-1.36''$
XMMU J0302.2-0001	CAHA 3.6 m† /Omega2000 imag.	50 min/23 min		2006 Jan. 3, 4	H/z	$1.34''/1.49''$
XMMU J0302.2-0001	VLT/FORS2 imag.	20 min	079.A-0119	2007 Feb. 23	R	$0.7''$
XMMU J1532.2-0836	VLT/FORS2 imag.	16 min/8 min	078.A-0265	2008 Apr. 4, 7	R/z	$0.6''/0.8''$

Notes. The grism column applies for spectroscopic observations, the band for imaging. Exposure times and seeing are reported for each band individually. $^{(\dagger)}$ Calar Alto Observatory.

of SAS (v10.0). The details of the observations are summarized in Table 1.

XMMU J0302.2-0001

XMMU J0302.2-0001 was detected in the *XMM-Newton* observation OBSID: 0041170101 with 39.3 ks PN exposure time and 50.4 ks in either MOS camera. We identified and excised a time period strongly affected by soft proton flaring in a two-step cleaning process yielding 36.4 ks PN and 46.2 ks MOS clean exposures. We find no residual quiescent soft proton contamination in any of the detectors.

The source is detected at the coordinates $(\alpha, \delta) = (03^{\rm h}02^{\rm m}11.9^{\rm s}, -00°01'34.3'')$ (J2000) at a relatively high off-axis angle of $11'$ with very high detection and extent significance (both $\gtrsim 10\sigma$). The beta model core radius is $r_{\rm C} = 14.4''$, based on a fit with a fixed $\beta = 2/3$. In an aperture of $1'$ we detected 130 source counts in PN and 80 in the combined MOS detectors.

XMMU J1532.2-0836

The second X-ray source, XMMU J1532.2-0836, is found in two *XMM-Newton* observations (OBSID: 0100240701 and 0100240801) at coordinates $(\alpha, \delta) = (15^{\rm h}32^{\rm m}13.0^{\rm s} -08°36'56.9'')$. The off-axis angles are in both observations similar, $\sim 5'-6'$. Pointing 0100240801 is slightly deeper with 19.4/25.7 ks clean time in PN/MOS compared to 13.2/17.3 ks of 0100240701. Unfortunately, after inspecting the light curve of observation 0100240801 we find a steady decline of the count rate along the whole duration of the observation – a clear indication of a residual quiescent (i.e. non-flaring) soft proton contamination. To confirm this suspicion we use a diagnostic test suggested by De Luca & Molendi (2004). By looking at the count rate ratio inside and outside the field of view of each detector in the 8−10 keV band, we find a ∼50% soft background enhancement compared to the normal level in PN and more than 90% enhancement in both MOS cameras. Observation 0100240701 is found to be completely uncontaminated. In both observations we detect below 50 source counts, which is reflected in the uncertainty of derived parameters.

The system was detected at a $\sim 5\sigma$ significance level, however it was classified as a point source in observation 0100240701. It is only in the slightly deeper (but contaminated) observation, where the source is flagged as extended with a 2σ significance and beta model core radius of $r_{\rm C} \simeq 8''$. Therefore, in the source detection step the extent is established only tentatively. We describe an in-depth investigation of the extent significance in Sect. 3.2, where we conclude that the currently available data is not sufficient to confirm the extended nature of the source with any statistical significance. All quoted values for XMMU J1532.2-0836 will come from the analysis of the uncontaminated field 0100240701, unless noted otherwise.

XMMU J0302.1-0000

We also identified an additional cluster candidate in the first *XMM-Newton* observation (OBSID: 0041170101) roughly $2'$ from XMMU J0302.2-0001. We obtained spectroscopy for member galaxies for both clusters simultaneously in the same FORS2 pointing. This allowed us to confirm also this second source, XMMU J0302.1-0000, as a genuine cluster of galaxies at intermediate redshift $z \approx 0.65$. In the following we will focus on the two $z > 1$ clusters and we provide details for XMMU J0302.1-0000 in Appendix A.

2.2. Optical/near-infrared observations

In addition to the archival X-ray data, we have obtained optical/near-infrared imaging and deep optical spectroscopy for the clusters. In this section we provide the details of the available data and its analysis.

2.2.1. Follow-up imaging and optical properties

The optical/near-infrared imaging data used in this work is summarized in Table 2. This data was obtained prior to spectroscopy to allow pre-selection of the cluster candidates. Here we use it to investigate the basic optical properties of the clusters' galaxy populations.

XMMU J0302.2-0001

In order to identify the optical counterparts of XMMU J0302.2-0001, we carried out medium deep H and z-band imaging data with the prime-focus wide-field (field-of-view of $15.4'$ on the side) near-infrared OMEGA2000 camera (Bailer-Jones et al. 2000) at the 3.5 m Calar Alto telescope. The observations were performed on 3rd and 4th January (H and z band respectively) 2006 under clear conditions (calibration with on-chip 2MASS stars was done in photometric conditions). We reduced the data with the designated OMEGA2000 NIR pipeline (Fassbender 2008). The individually reduced frames are visually checked and co-added. The total exposure time of the final stacked images is 50 min in H band (75 co-added frames) and 23 min in z band (23 frames). We reach a 50% completeness limit (AB) of $H_{\rm lim} = 22.4$ mag and $z_{\rm lim} = 23.5$ mag with $FWHM(H) = 1.34''$ and $FWHM(z) = 1.49''$.

The photometry catalog was obtained by running `SExtractor` (Bertin & Arnouts 1996) in dual image mode with the unsmoothed H-band image used as the detection image. We then cross-checked the catalog with available SDSS photometry.

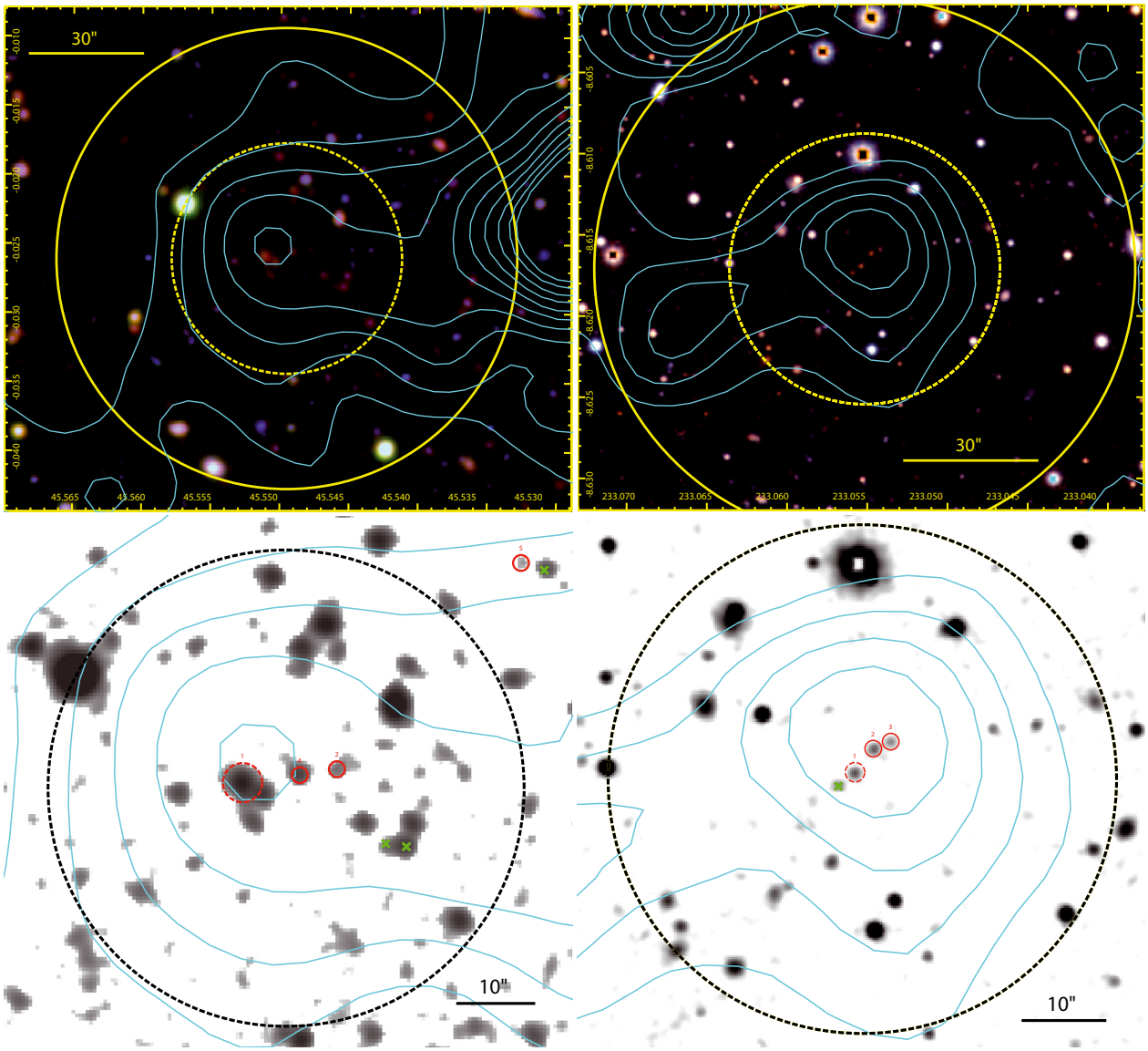

Fig. 1. Optical/Near-Infrared images of the clusters. *Top*: pseudo-color image of the clusters XMMU J0302.2-0001 (*left*, red channel: H band, green: z, blue: R) XMMU J1532.2-0836 (*right*, red channel: z, green: $z + R$, blue: R). Adaptively smoothed X-ray contours are overlaid in cyan. Solid/dashed circles mark a 60″/30″ radius region centered on the X-ray detection. An associated overdensity of red galaxies is apparent in both cases. *Bottom*: a high contrast zoom on the central regions of the clusters (dashed circle has a 30″ radius). XMMU J0302.2-0001 is displayed in the H band whereas XMMU J1532.2-0836 in the z band. Red circles mark the confirmed spectroscopic members with properties listed in Table 3 and spectra displayed in Fig. 3. The BCG is marked with a dashed red circle (ID 1 for both clusters). Spectroscopically confirmed foreground galaxies are indicated by green crosses.

The VLT/FORS2 imaging (Prog. ID: 079.A-0119(A)) was carried out in the R-band at a fairly good seeing of ∼0.7″ and photometric conditions. With total clean exposure time of 20 min, it is a valuable complement to the Calar Alto imaging data. For the reduction of the pre-imaging data we followed the same procedure as Schwope et al. (2010) and Fassbender et al. (2011a).

In Fig. 1 (top left) we display a pseudo-color image of XMMU J0302.2-0001 in the $H/z/R$ bands (red/green/blue). A population of red galaxies ($1.45 < z - H \leq 2.15$) is found to be coincident with the X-ray source. We show the $z - H$ vs. H color−magnitude diagram (CMD) of XMMU J0302.2-0001 in Fig. 2 (top). We also overplot the synthetic $z - H$ color of a Simple Stellar Population (SSP) model (formation redshift $z_f = 5$, solar metallicity) for the cluster's redshift (red dashed line). We find around 10 red galaxies within 30″ from the X-ray center with colors well matching the model prediction. The overdensity of red galaxies compared to the field is at a ∼25σ significance level – one of the largest known overdensities at $z > 1$.

The brightest cluster galaxy (BCG) is coincident with the X-ray emission peak and seems to be undergoing merging activity (see Fig. 1, bottom left). The very bright blue object ($H \approx$ 18.4 mag) at the cluster redshift (but beyond 30″ from its center) is an AGN with redshift from SDSS (Sect. 3.4). Galaxy ID: 6 (in Table 3) also has a bluer color, which is consistent with the presence of a very strong [O II] emission line (see Fig. 3).

XMMU J1532.2-0836

The imaging in the case of XMMU J1532.2-0836 consists of R and z band imaging obtained with the VLT/FORS2 instrument

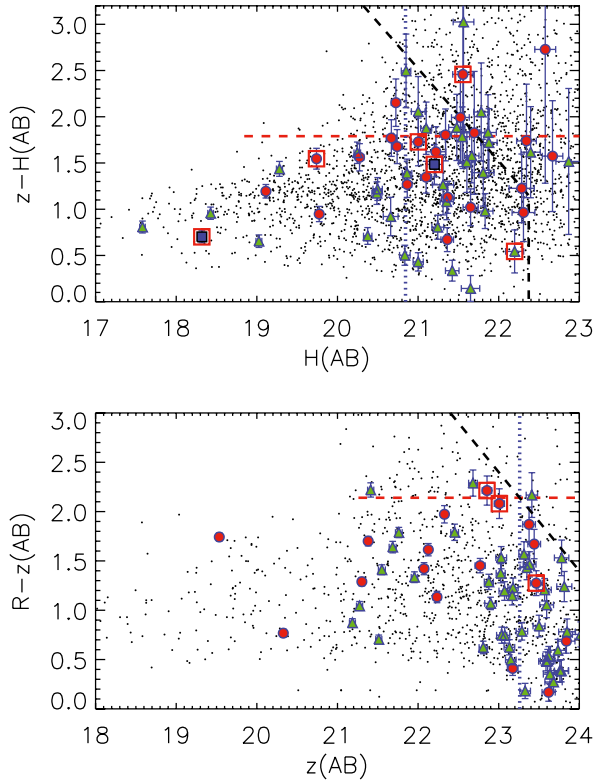

Fig. 2. *Top*: the $z - H$ vs. H color−magnitude diagram (CMD) for XMMU J0302.2-0001. Square boxes mark secure spectroscopic cluster members. Galaxies with projected cluster-centric distances less than 30″ are shown as red circles, those with distances between 30″–60″ as green triangles. Galaxies with concordant redshift at >60″ distances have blue squares. The dashed black line marks the magnitude limits. The apparent H band magnitude of an L^* galaxy at the cluster redshift is shown with a vertical blue dotted line. To help to guide the eye we overplot the color of a solar metallicity SSP model for the clusters' redshifts with formation redshift $z_f = 5$ (horizontal red dashed line). *Bottom*: the $R-z$ vs. z CMD of XMMU J1532.2-0836. The symbols and colors have the same meaning as in the above plot. Two of the spectroscopic members lay on the model prediction for a red sequence at this redshift, the third member has a significantly bluer color.

(Prog. ID: 078.A-0265) and seeing of 0.6″ and 0.8″, respectively. The total exposure time is 16 min in R band and 8 min in z. The final $R - z$ vs. z color−magnitude diagram of XMMU J1532.2-0836 is displayed in Fig. 2 (bottom). The dashed red line shows the $R - z$ color of a spectro-photometric sequence (SSP model, $z_f = 5$, solar metallicity) at the redshift of the cluster. Two spectroscopic members have colors consistent with this simple model.

As can be noted from the figure, these two galaxies are very close to the completeness limit of our data and we can thus see only the very brightest end of the galaxy population. The third galaxy (ID: 3) has bluer colors and a strong [O II] emission line. We also detect [Ne III]λ3869 Å and [Ne V]λ3426 Å emission lines. It is therefore likely that this galaxy harbours an obscured AGN (see Sect. 3.2).

We have designated the brightest spectroscopic member as the cluster candidate's BCG (ID: 1), with ∼5.5″ distance from the cluster center. This galaxy is relatively faint ($z^* - 0.4$). The brightest galaxy lying exactly at the predicted SSP color is a spectroscopically confirmed foreground galaxy. However, there is one galaxy slightly brighter than the marked BCG within 30″ from the X-ray center – which could also be a BCG candidate. Unfortunately, we do not have spectroscopy for this source. Compared to galaxy ID: 1 it has a slightly bluer color than the SSP prediction and a slightly larger cluster-centric distance, i.e. ID: 1 still remains the better BCG candidate.

2.2.2. Spectroscopic confirmation

In order to increase the efficiency of spectroscopic follow-up, we submit the X-ray identified candidates to a pre-screening process based on optical/near-infrared imaging. This allows us to compile a candidate shortlist with very low contamination rate (Fassbender 2008).

XMMU J0302.2-0001 was classified as a good high redshift cluster candidate based on its solid X-ray detection and a very prominent (∼25σ) overdensity of red galaxies. This system was therefore selected as a prime candidate for spectroscopic follow-up.

For XMMU J1532.2-0836, the depth of the available X-ray observations allowed us to establish it only as tentative high-z cluster candidate. However, the optical images revealed four very red galaxies exactly coincident with the X-ray emission peak and thus also this system was included among the cluster candidates for the purpose of spectroscopic confirmation with the VLT/FORS2 instrument.

For each cluster we carried out an observation in the MXU-mode (Mask eXchange Unit), whose 6.8′ × 6.8′ field-of-view allows us to obtain a sufficient number of galaxy spectra with a single slit mask centered on the cluster.

We reduced the observations with a new FORS 2 adaptation of the VIMOS Interactive Pipeline and Graphical Interface (VIPGI, Scodeggio et al. 2005) which includes all the standard analysis steps – bias subtraction, flat field corrections, image stacking and extraction of background subtracted 1D galaxy spectra. The wavelength calibration is carried out using a helium-argon lamp reference line spectrum (calibration uncertainty <1 Å). Details of the spectroscopy reduction pipeline will be given in Nastasi et al., in prep. The final stacked spectra are corrected for the sensitivity function of the FORS 2 instrument. We obtain the galaxy redshifts by cross-correlating their spectra with a galaxy template library using the IRAF[3] package RVSAO and the EZ software (Kurtz & Mink 1998; Garilli et al. 2010, respectively). The redshifts are thus determined by taking into account the shape of the continuum and all possible features (even those with low individual detection significances) rather than just a few most significant absorption/emission features.

XMMU J0302.2-0001

As can be seen in Fig. 3 (bottom, left), there is a peak of six concordant redshifts in the galaxy redshift distribution around the X-ray center of XMMU J0302.2-0001 at $z \approx 1.19$. The measured redshifts, the most dominant spectral features and cluster centric distances are listed in Table 3. Five of the galaxies are within 55″ from the X-ray center. This includes also the BCG and two additional red galaxies in the immediate vicinity of the X-ray centroid (<10″ offset, see Fig. 1), which allows us to establish the redshift of the system with good confidence. The spectra of galaxies ID: 4 and ID: 5 have low signal-to-noise ratios, but we still are able to measure their redshifts rather safely and keep them therefore in the member list. Galaxy ID: 6 is not passive – it exhibits an extremely strong [O II] emission line.

[3] `iraf.noao.edu`

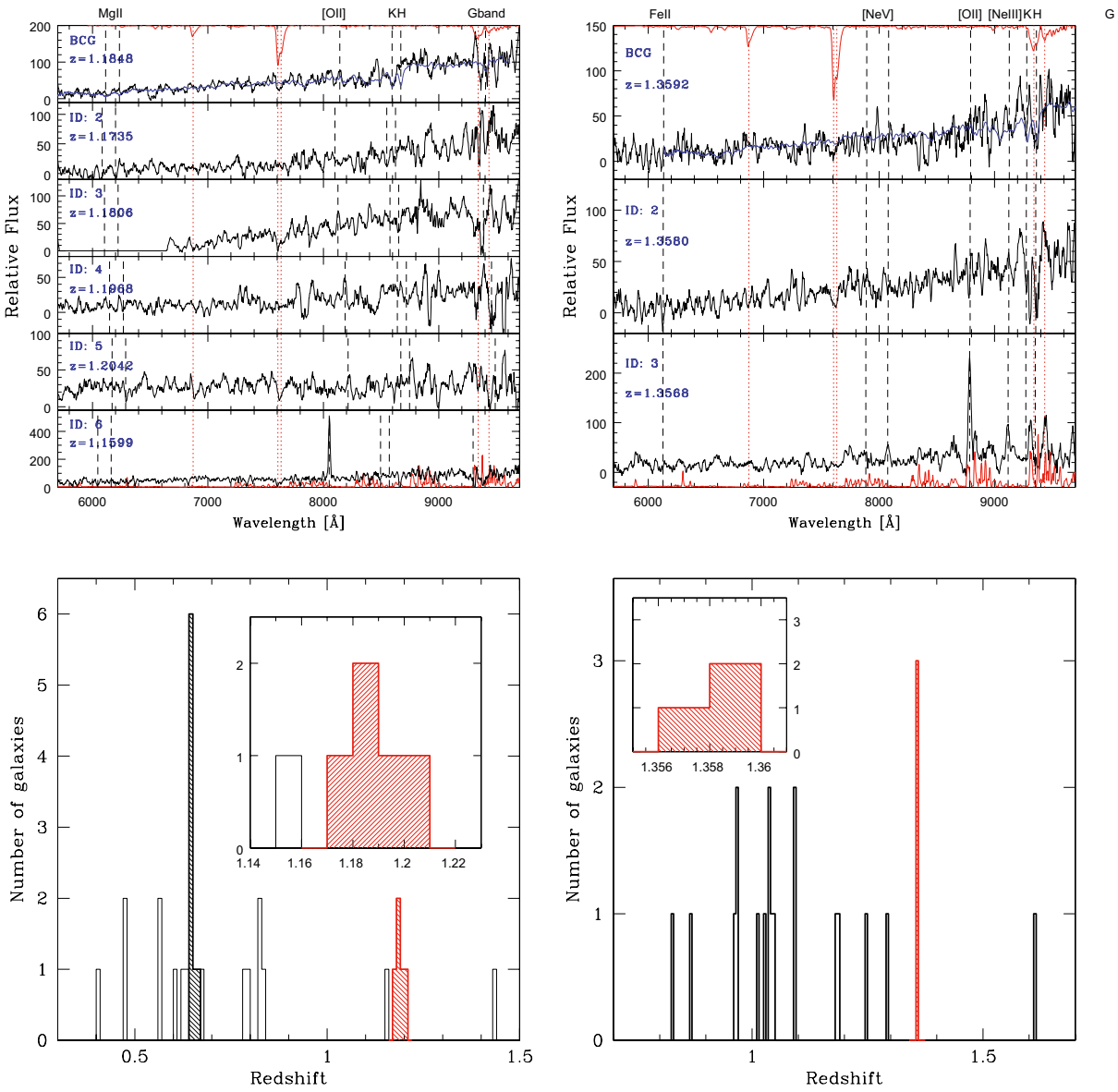

Fig. 3. *Top*: spectra of secure cluster members for XMMU J0302.2-0001 (*left*, $z = 1.185$) and XMMU J1532.2-0836 (*right*, $z = 1.358$) smoothed with a 7 pixel boxcar filter. The expected observed positions of prominent spectral features at the median redshift are indicated by black dashed lines. The sky spectrum (*bottom*) and telluric features (*top*) are overplotted in red. For the BCGs (*top panels*) we display an overlaid LRG template spectrum in blue. *Bottom*: distribution of VLT/FORS2 galaxy spectra for the two clusters. The red hashed parts show the distribution of the red galaxies for both clusters (also shown in the insets), selected by requiring the redshift to be within $z_{\rm CL} \pm 0.015$. The black hashed peak in *the left panel* (at $z \approx 0.65$) corresponds to cluster XMMU J0302.1-0000 (see Appendix A). See also Sect. 2.2.2 for discussion.

Table 3. Spectroscopic redshifts of cluster member galaxies.

ID	α (J2000)	δ (J2000)	$z_{\rm spec}$	$d_{\rm X}$ [″]	Features
XMMU J0302.2-0001					
1 (BCG)	03:02:12.260	–00:01:33.87	1.1848 ± 0.0007	5.4	[O II]†, Ca-K, 4000 Å break
2	03:02:11.462	–00:01:32.01	1.1735 ± 0.0007	7.0	Mg II, Ca-H/K, 4000 Å break
3	03:02:16.181	–00:03:32.28	1.1806 ± 0.0004	134.3	[O II], Ca-H/K†
4	03:02:11.774	–00:01:32.61	1.1968 ± 0.0007	2.5	Mg II, [O II], Ca-H, G band
5	03:02:09.930	–00:01:05.91	1.2042 ± 0.0004	41.0	[O II]†
6	03:02:15.228	–00:01:49.87	1.1596 ± 0.0004	52.3	[O II]
XMMU J1532.2-0836					
1 (BCG)	15:32:13.294	–08:37:00.75	1.3592 ± 0.0016	5.5	Mg II, Ca-H/K
2	15:32:13.149	–08:36:57.97	1.3580 ± 0.0007	2.1	Fe II, Mg II, Ca-H/K
3	15:32:13.010	–08:36:57.14	1.3568 ± 0.0005	0.4	Fe II, [O II], [Ne III], [Ne V]

Notes. The last column lists the main detected spectral features. Forbidden lines are detected in emission, the rest in absorption. The distance from the X-ray center in arcseconds is given as the $d_{\rm X}$ parameter. $^{(\dagger)}$ The feature is faint.

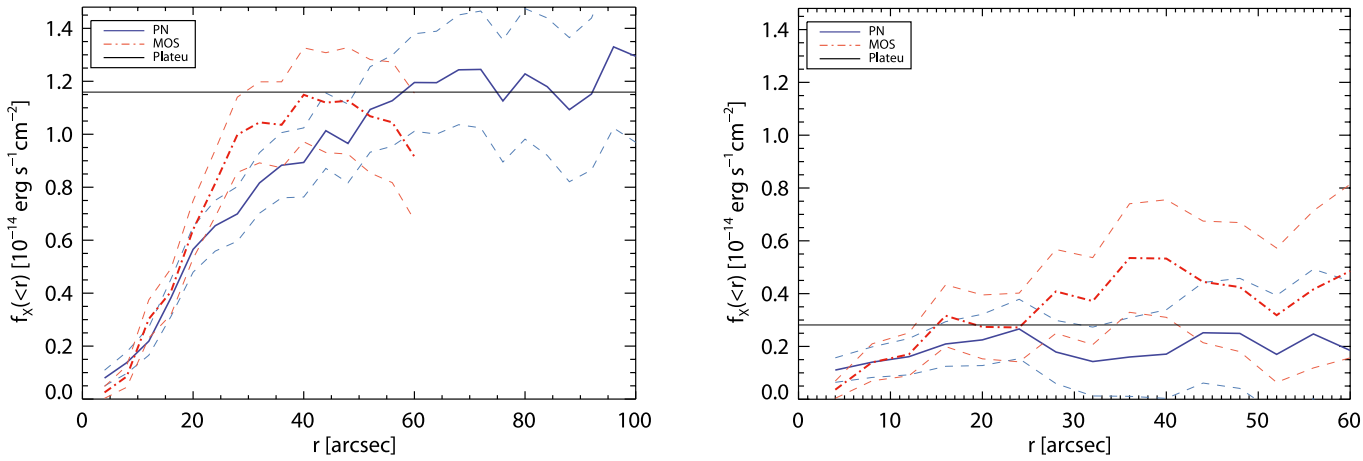

Fig. 4. Growth curve analysis of XMMU J0302.2-0001 (z = 1.185, *left*) and XMMU J1532.2-0836 (z = 1.358, *right*). The curves show the encircled cumulative flux as a function of radius (PN: blue curve, combined MOS: red, dot-dashed). Dashed lines mark the flux measurement error bars which include the Poisson noise and an additional 5% systematic error from the background estimation. The horizontal lines mark the plateau levels. See Sect. 2.3 for details.

In order to estimate the final cluster redshift we apply a selection criterion adopted from Milvang-Jensen et al. (2008): we require the galaxy redshifts to be in a 0.015 wide redshift slice around the iteratively established cluster redshift. This selection includes galaxies ID: 1−5 and yields a median cluster redshift of $z = 1.185 \pm 0.016$ (error is the interquartile range).

We conclude the discussion of the spectroscopy of XMMU J0302.2-0001 by remarking that there is an additional spectroscopic galaxy redshift from the Sloan Digital Sky Survey which is concordant with the cluster redshift. We discuss this source in Sect. 3.4.

XMMU J1532.2-0836

For XMMU J1532.2-0836 we were able to obtain three galaxy spectra (Fig. 1, top right). All the three spectra have good signal-to-noise ratios and the redshifts can be anchored by several prominent spectral features (Table 3). They yield a redshift of the system equal to 1.358 ± 0.001. The three spectroscopic members are within ∼6″ from the X-ray center (Fig. 1, bottom right). The fourth red galaxy close to the center was found to be a foreground object.

Galaxy ID: 3 has a very prominent [O II] emission line and [Ne III] and [Ne V] lines were detected as well. These features are characteristic for the population of obscured AGN (e.g. Groves et al. 2006). The implications of the presence of an AGN for the X-ray analysis of the source is discussed in Sect. 3.1.

Finally, we note that the redshift distribution in Fig. 1 exhibits also a peak at $z \approx 1.1$ (four concordant galaxy redshifts). These galaxies are, however, spread over the whole field (i.e. are spatially unrelated) and thus do not form a genuine system.

2.3. Growth curve analysis of the X-ray imaging data

We utilize an improved version of the *growth curve method* (Böhringer et al. 2000), in order to trace the emission to an as high cluster-centric distance as possible and obtain a reliable measurement of the flux. The cumulative source flux (i.e. background-subtracted) as a function of radius, the growth curves, for the two systems are displayed in Fig. 4. The total source flux was determined iteratively by fitting a line to the flat part of the background-subtracted growth curve. We define the *plateau radius* ($r_{\rm plat}$) as the aperture where the growth curve levels off into a flat plateau. The flux at this radius is the total detected flux of the source.

XMMU J0302.2-0001

For XMMU J0302.2-0001 we found $r_{\rm plat} = 55''$, $F_{\rm plat}$ (0.5–2.0 keV) = $(11.73 \pm 1.36) \times 10^{-15}$ erg s^{-1} cm^{-2} and a total luminosity $L_{\rm plat}(0.5–2.0\ {\rm keV}) = (8.56 \pm 0.99) \times 10^{43}$ erg s^{-1} (Fig. 4). Errors of the flux and luminosity include the Poisson errors and a 5% systematic error in the background estimation.

The analysis of this cluster is complicated by the presence of an extremely bright point source 80″ away from the cluster center. At this high off-axis angle the point-spread function (PSF) is already significantly broadened with respect to its on-axis shape and therefore the emission of the point source is spread out in the PSF wings inside the cluster region. Before the background estimation we manually removed a circular region with a conservative radius centered on the point source. The flux estimation described above is based on images with the point source masked out in the same way. We have mitigated this contamination of the cluster emission by excluding these regions and extrapolating the cluster emission as measured at the same cluster-centric radius but from the uncontaminated parts.

XMMU J1532.2-0836

We display the growth curve for XMMU J1532.2-0836 in Fig. 4 (right) extracted from the uncontaminated field (OBSID: 0100240701, see Sect. 2.1). We detected the source emission out to $r_{\rm plat} = 22''$, with a total source flux of $F_{\rm plat}(0.5–2.0\ {\rm keV}) = (2.82 \pm 1.11) \times 10^{-15}$ erg s^{-1} cm^{-2}, i.e. four times fainter than XMMU J0302.2-0001. This flux at the cluster's redshift corresponds to a total luminosity $L_{\rm plat}(0.5–2.0\ {\rm keV}) = (3.59 \pm 1.41) \times 10^{43}$ erg s^{-1}. We note that the source is very faint and thus the flux could be established only with a ∼40% error. A systematic shift between the MOS and PN is also apparent in Fig. 4 (the MOS flux being higher). Note however, that the growth curves are cumulative flux distributions and thus the radial bins are not independent. All subsequent physical parameters are thus only tentative

and will require a dedicated deeper (on-axis) X-ray observation for corroboration.

Except for pointing 0100240701 there is an additional *XMM-Newton* observation available of similar depth and at similar off-axis angle, but this one is heavily contaminated by soft-protons. There is some evidence that the soft protons undergo reflection on the telescopes mirror and are thus vignetted across the field of view. The vignetting function for MOS was tentatively established by Kuntz & Snowden (2008) to be shallower than the vignetting of genuine X-ray photons. For PN a systematic study has not yet been carried out but a preliminary analysis suggests a similar shape to the MOS vignetting. Given this, our two-component background model should be able to capture the enhanced background to the first order. We have therefore extracted growth curves also from the second observation. We find that while there is a relatively large scatter between the curves, they typically agree within the error bars. The measured total flux (the plateau level of the curves) agree very well, the difference between them being much smaller than their errors: $F_{\rm plat}(0100240701) = 2.82 \pm 1.11$ and $F_{\rm plat}(0100240801) = 2.95 \pm 0.94$ in 10^{-15} erg s^{-1} cm^{-2} units in the 0.5−2.0 keV band. This is a reassuring indication that indeed the plateau fitting algorithm and the procedure of combining the growth curves from PN and MOS yields very stable results, even for observations with non-standard backgrounds.

3. Results and discussion

3.1. Physical properties of the clusters

The number of counts for both clusters is insufficient for a spectroscopic analysis and therefore we can estimate additional physical parameters only through luminosity based scaling relations. In the following analysis, we will assume that the entire X-ray emission detected and characterized by the growth curve analysis (Sect. 2.3) originates in the ICM (after removing the detected point sources). For XMMU J0302.2-0001 we find no indication that there is any further contamination, but in the case of XMMU J1532.2-0836 this assumption is likely not valid due to the presence of an obscured AGN (Sect. 2.2.2). We discuss this possibility in Sect. 3.2. The physical parameters for this system should therefore be considered as upper limits.

Due to the high redshift of the clusters and the limited resolution of *XMM-Newton* we can not excise the core regions of the clusters. We therefore use the scaling relations that include cores. We use the growth curve (Böhringer et al. 2000) to iteratively obtain a self-consistent set of parameters utilizing luminosity based scaling relations. The iterative procedure is described in Šuhada et al. (2010), with the difference that we extrapolate the 0.5−2 keV luminosity to obtain its bolometric value. We estimate the remaining physical parameters using the bolometric $L - T$ and $L - M$ relations from Pratt et al. (2009) (orthogonal fit, no Malmquist bias correction).

First, we assume a self-similar evolution of the scaling relations. Under this assumption, we estimate the objects to be intermediate mass systems with $M_{500} \simeq 1.2 \times 10^{14}\ M_{\odot}$ for XMMU J0302.2-0001 and $M_{500} \simeq 7 \times 10^{13}\ M_{\odot}$ for XMMU J1532.2-0836. This corresponds to temperatures $T \simeq 3$ keV and $T \simeq 2$ keV respectively. The results for both systems are summarized in Table 4.

The major uncertainty on the estimated physical parameters at these high redshifts stems from the fact that the evolution of the scaling relations is not yet well established. Self-similar evolution is a common assumption and a direct prediction of the simple, purely gravitation driven growth. However there are several indications that the evolution of luminosity scaling relations is slower than the self-similar prediction – see discussion in Fassbender et al. (2011a) and references therein, e.g. Stanek et al. (2010) and Reichert et al. (2011).

We therefore adopt the simplified approach of Fassbender et al. (2011a) and remove a factor of $E(z)$ from the self-similar evolution factor ($E(z)^{-7/3}$) in the bolometric luminosity based scaling relations. This modified evolution factor, $E(z)^{-4/3}$, is consistent with preliminary results of Reichert et al. (2011) based on a fit to a large sample of high redshift clusters compiled from the literature. Since our algorithm iteratively estimates a self-consistent set of parameters, the change of scaling relations impacts slightly the estimated flux and luminosity (mainly through the temperature dependence of the energy-conversion-factor). This change is minuscule, but for consistency we display the full sets of the estimated parameters for both calculations (i.e. the self-similar and no-evolution scenarios) in Table 4.

However, the impact of the different evolution models on temperatures and masses is serious. The non-evolving case approach yields roughly 30% higher cluster masses and ∼25% higher temperatures (Table 4, bottom). Given the precision of the scaling relations (and their intrinsic scatter) and the error of the luminosity measurement, the estimates are still in agreement within their 1σ error bars (albeit for the masses only barely). However, this uncertainty is systematic and very important for studies of cluster samples (and naturally the eventual cosmological constraints derived from them). This clearly demonstrates the importance of establishing a well controlled high-redshift calibration cluster sample.

For both the self-similar and no-evolution scenarios we also include our estimates of the mass M_{200} (mass inside the aperture where the mean density is 200 times the critical density of the Universe). The masses have been obtained by extrapolating M_{500} assuming an NFW profile (Navarro et al. 1997) and using the relations of Hu & Kravtsov (2003) and the DM profile concentration mass/redshift dependence of Bullock et al. (2001). The parameters are obtained iteratively using the M_{500} values as inputs. For both clusters the conversion factor $M_{500} \mapsto M_{200}$ is ≈1.5 and M_{200} is ∼90% of the virial mass.

While at their observed redshifts the clusters would rank among intermediate and low mass systems, respectively, they still have ∼8−9 Gyr of potential mass accretion ahead, before reaching the current epoch. In order to predict the final mass of the clusters at $z = 0$, we use the mean mass growth rate relations of Fakhouri et al. (2010), based on the mass assembly histories of halos in the Millennium and Millennium-II simulations. We estimate the $z = 0$ mass of XMMU J0302.2-0001 to be $1 \times 10^{15}\ M_{\odot}$ and $7 \times 10^{14}\ M_{\odot}$ for XMMU J1532.2-0836. Thus at the present epoch, XMMU J0302.2-0001 would be a very massive clusters with a mass similar to the Coma cluster. If we use the definition of formation time as the redshift at which the cluster acquired 50% of its $z = 0$ mass (e.g. see the Appendix of Giocoli et al. 2007), the formation redshift of XMMU J0302.2-0001 would be around $z \approx 0.5$, while XMMU J1532.2-0836 would be assembled slightly earlier, at $z \approx 0.6$.

3.2. The nature of the X-ray emission of XMMU J1532.2-0836

XMMU J1532.2-0836 with its flux $F_{\rm X} \approx 3 \times 10^{-15}$ erg cm^{-2} s^{-1} is one of the faintest cluster candidates discovered in a serendipitous X-ray survey. Given the estimated upper limits, we are

Table 4. Basic X-ray parameters of XMMU J0302.2-0001 and XMMU J1532.2-0836.

Parameter	XMMU J0302.2-0001	XMMU J1532.2-0836[a]	Units
α (J2000)[b]	$03^h02^m11.9^s$	$15^h32^m13.0^s$	
δ (J2000)[b]	$-00°01'34.3''$	$-08°36'56.9''$	
redshift	1.185 ± 0.016	1.358 ± 0.001	
$E(z)$	1.96	2.15	
Ang. scale	8.28	8.41	kpc s^{-1}
n_H[a]	7.07	8.13	10^{20} cm^{-2}
$L-M$, $L-T$ **self-similar evol.**			
F_{500} [0.5–2.0 keV]	11.44 ± 1.28	3.02 ± 0.96	10^{-15} erg cm^{-2} s^{-1}
L_{500} [0.5–2.0 keV]	8.35 ± 0.93	3.81 ± 1.21	10^{43} erg s^{-1}
F_{500} [bolometric]	13.62 ± 2.96	3.52 ± 2.46	10^{-15} erg cm^{-2} s^{-1}
L_{500} [bolometric]	21.08 ± 2.36	8.63 ± 2.75	10^{43} erg s^{-1}
T_{500}	2.8 ± 0.7	2.1 ± 0.6	keV
M_{500}	1.2 ± 0.2	0.7 ± 0.2	10^{14} $M_\odot$
r_{500}	0.47	0.37	Mpc
M_{200}	1.7 ± 0.4	1.0 ± 0.3	10^{14} $M_\odot$
$L-M$, $L-T$ **no evol.**			
F_{500} [0.5–2.0 keV]	11.59 ± 1.33	2.89 ± 1.14	10^{-15} erg cm^{-2} s^{-1}
L_{500} [0.5–2.0 keV]	7.80 ± 0.90	3.23 ± 1.27	10^{43} erg s^{-1}
F_{500} [bolometric]	12.93 ± 3.14	3.51 ± 2.72	10^{-15} erg cm^{-2} s^{-1}
L_{500} [bolometric]	21.62 ± 2.50	7.82 ± 3.03	10^{43} erg s^{-1}
T_{500}	3.5 ± 0.9	2.6 ± 0.7	keV
M_{500}	1.6 ± 0.3	0.9 ± 0.3	10^{14} $M_\odot$
r_{500}	0.53	0.42	Mpc
M_{200}	2.5 ± 0.5	1.4 ± 0.4	10^{14} $M_\odot$

Notes. Flux and luminosity errors include the Poisson errors and a 5% systematic error in the background estimation. Errors of parameters obtained from scaling relations include the measurement errors of the luminosity and temperature, respectively, and the intrinsic scatter of the scaling relations. The first set of parameters uses the self-similar $L-T$ and $L-M$ relations from Pratt et al. (2009) for the bolometric luminosity. The second set of parameters (the no-evolution case) follows the prescription of Fassbender et al. (2011a) by removing one $E(z)$ factor from the bolometric luminosity scaling relations of Pratt et al. (2009). In both scenarios, scaling relations are obtained by the BCES orthogonal fit algorithm (Akritas & Bershady 1996) and the input luminosities include the core regions. Parameters for XMMU J1532.2-0836 are upper limits. See Sect. 3.1 for more discussion. [(a)] All values are upper limits; [(b)] X-ray coordinates based on a maximum-likelihood fit of a PSF-folded beta model to the surface brightness distribution; [(c)] values from the LAB HI survey (Kalberla et al. 2005).

indeed entering here the low-mass cluster/group regime at high redshifts. Probing the feasibility limits of this kind of cluster surveys, however also means that we have to deal with increasing uncertainty in the sources' classification and characterization.

In this case, the initial detection revealed the presence of an extended source at $\sim 2\sigma$ significance level (but only in one of the two observations). Optical/near-infrared imaging confirmed the presence of red galaxies coincident with the X-ray detection and spectroscopic data confirmed the presence of a dynamically bound galaxy system.

Optical spectroscopy, however, also revealed the likely presence of an obscured AGN in the core of the cluster (Sect. 2.2.2). The X-ray spectral distribution of an AGN can in first approximation be described as a power-law (with average index $\Gamma \approx 1.8$) intrinsically absorbed with hydrogen column densities from $\sim 10^{22}$ cm^{-2} to over 10^{25} cm^{-2} (for Compton thick sources) depending on the structure and orientation of the circumnuclear absorber (e.g. Antonucci & Miller 1985). This local absorption introduces a photoelectric absorption cut-off removing most of the soft X-ray emission. Unfortunately, for an AGN at redshift $z = 1.358$ a significant fraction of photons are redshifted from unabsorbed parts of the spectrum into our detection band (0.5–2 keV). Intrinsic absorption column densities equal to a few times 10^{23} cm^{-2} are enough to remove a significant fraction of the soft emission even after redshifting and thus for these cases the AGN contamination of the observed X-ray emission should be small or even negligible. However, for lower column densities the AGN emission would give a significant contribution and indeed possibly be even the dominant source of the detected photons.

Since the observations are not deep enough to constrain the source spectrum, we have checked the hardness ratios (ratio of the difference of counts in two adjacent bands) of the source in our detection bands (0.3–0.5, 0.5–2 and 2–4.5 keV). Due to the faintness of the source the ratios are highly uncertain, but are consistent with ICM emission. Given the uncertainties, however, AGN contamination (assuming moderate absorption) can also not be ruled out this way.

Apart from the spectral distribution, a safe detection of source extent would constitute a strong piece of evidence that the observed emission originates from the thermal bremsstrahlung of the ICM. As discussed in Sect. 2.1 source extent was detected only in the slightly deeper, but contaminated field. We re-examine the shallower, clean observation 0100240702 looking for instrumental effects that could mask the source's true extent. In this observation the source lies partially in a very prominent out-of-time (OoT) event stripe (in the PN detector) caused by the very bright star system (UZ Lib) which was the actual target of the observation. Originally, we removed the OoT stripe in the observation in a standard, statistical way[4]. We then try an

[4] See e.g. the *XMM-Newton* user handbook, `xmm.esac.esa.int/sas/current/doc/`.

alternative approach, by keeping the OoT events in the detection images and modelling them in the background estimation step. This method also does not yield an extent detection.

The area around the system is strongly affected by chip gaps in the MOS detectors. In the next run we therefore applied a much less conservative criterion for including low exposure areas in the vicinity of chip gaps, gaining thus more geometric area for source detection. With this modification the source is still detected without a significant extent.

As a final test, we carry out a joint source detection on both fields simultaneously (i.e. two times three detectors, each in three bands). The joint detection is carried out in two different ways. First we stack the data from the same detectors/bands and run source detection simultaneously on the nine merged data sets. XMMU J1532.2-0836 is detected in the merged data set with a higher detection significance as in either of the single observations, but its extent is not confirmed.

Merging observations has the disadvantage that the exact information on the shape of the point-spread-function (PSF) is lost (the two observations have slightly different off-axis and position angles. While the effect is expected to be small, it could be a deciding factor in this case, since the potentially extended emission is so weak. Therefore we also attempt to carry out source detections on all 18 images[5] simultaneously without stacking them. There is currently no SAS task that can carry out extended source detection in two pointings simultaneously, but we modified the source code of the `emosaicproc` task (experimental task in SAS v10.0.0, originally developed for point source detection in mosaic observations) to fit our purposes. However, also this approach does not yield a detection of extent at a statistically significant level. We repeated the procedures for several possible combinations of detectors with no extent detections in most of the cases. Extent was detected exclusively in runs where the two MOS detectors from the contaminated observations were used along with either of the PN cameras. Given that these MOS detectors have the highest contamination (~90% compared to 50% of the PN from this same observation) it leads us to the conclusion that the extent is likely due to an unaccounted background fluctuations caused by the soft-proton contamination. We estimate that for a fully conclusive confirmation of AGN presence a 25 ks *Chandra* observation will be sufficient (gathering ~25 source counts). Time for this follow-up observation has been allocated.

In summary, the extent of the source was not confirmed by deeper analysis. While XMMU J1532.2-0836 clearly constitutes a dynamically bound system, the detected X-ray emission can not be unambiguously attributed to the ICM from the available data. Note however, that we have below 100 source counts (after background subtraction) even if we combine both available observations. Given our findings we can not exclude the possibility that the detected AGN is the dominant (possibly only) source of X-ray emission detected from this system. This source is thus an example of systems that even with availability of multi-wavelength data are hard to properly classify. For large upcoming surveys such systems will be presumably numerous (e.g. *eRosita*, which in addition has a slightly worse PSF) and therefore additional studies will be needed to establish how can we explore the cluster-group transition regime at high redshifts with good confidence and effective use of follow-up observing time.

[5] Two observations times three detectors times three bands.

3.3. The galaxy population of the clusters

It is interesting to note that in the cluster XMMU J0302.2-0001 we detect [O II] line emission in four out five spectroscopic members (excluding the galaxy ID: 6). This feature, an indicator of sustained star-formation, is detected along with other features which are typical for mature systems. Similar activity is observed also in other high redshift X-ray selected clusters: XMMU J1007.4+1237 (at $z = 1.56$ Fassbender et al. 2011b), XMMU J0338.8-0030 (Pierini et al. 2011) and XMMU J2235.3-2557 (Lidman et al. 2008) at $z = 1.39$. While some of these [O II] emitters are bluer than the cluster red sequence, many of them have colors in full agreement with the old, passive galaxies and in some cases are even redder (e.g. in XMMU J2235.3-2557). These galaxies can also span a large range in magnitudes, up to the very bright end of the cluster luminosity function. An increase in star formation activity in red sequence galaxies is also apparent in optically selected cluster sample of Finn et al. (2010) (mostly intermediate redshift systems) and in dense galaxy environments at redshifts ~1 seen in GOODS and DEEP2 galaxy surveys (Elbaz et al. 2007; Gerke et al. 2007; Cooper et al. 2008).

We are thus very likely observing residual stochastic star-formation in probably bulge dominated disc galaxies. This effect can be expected to be more important as we move to higher redshifts and enter lower-mass regimes. As we have remarked in Sect. 3.1, based on cluster mass growth rates from simulations, XMMU J0302.2-0001 is still in its assembly phase and is expected to be experiencing significant mass accretion and merging activity. These processes lead to large variations in the cluster/group tidal field. Based on numerical simulations Martig & Bournaud (2008) show that tidal field fluctuation can enhance the star formation activity of galaxies (beyond the expectations from purely galaxy-galaxy interaction driven activity). This effect should be particularly efficient at high redshifts and in low mass systems, before quenching processes take place. The XDCP project has the X-ray sensitivity and sky area to be able to effectively study this transition regime and the relevant environmental effects. We leave further discussion to an upcoming dedicated study based on available data. However, we note that in order to completely disentangle the ongoing processes, information on the spectral energy distribution at $\lambda > 4000$ Å (rest frame) is necessary as well as high-spatial resolution imaging in order to be able to assess the galaxy morphologies.

3.4. Cross-correlation with known sources

We queried the NASA/IPAC Extragalactic Database[6] and the SIMBAD Astronomical Database[7], in search for potentially interesting known sources.

We find that XMMU J0302.2-0001 has been previously detected by the BLOX survey (Bonn lensing, optical, and X-ray selected galaxy clusters Dietrich et al. 2007) as the object BLOX J0302.2-0001.5. The cluster was selected in X-rays, but not by the optical and weak lensing detection algorithms. Their estimates of the X-ray parameters ($r_C = 12.8'' \pm 1.2''$ and flux $F_X = (12.1 \pm 1.3) \times 10^{-15}$ erg cm^{-2} s^{-1} in the 0.5–2 KeV band) are in good agreement with our values. The cluster does not have a redshift measurement from the BLOX survey.

At a cluster centric distance of ~185″ we find the source SDSS J030214.82+000125.3 identified in the Sloan Digital Sky

[6] `nedwww.ipac.caltech.edu`
[7] `simbad.u-strasbg.fr/simbad/`

Survey (SDSS) as a quasar (Véron-Cetty & Véron 2006). The object has a known spectroscopic redshift, $z = 1.179$ (Schneider et al. 2007; Cristiani et al. 1996), which is in concordance with our redshift for XMMU J0302.2-0001. At ∼185″ offset (corresponding to ∼1.5 Mpc at this redshift) it could be associated with the cluster's outskirt region. We also detect this quasar as a high significance X-ray point sources in our *XMM-Newton* observation (see Fig. A.3).

For the cluster XMMU J1532.2-0836 we do not find any complementary redshifts in the databases. Neither do we find any known radio source within a 2′ radius from either system.

Both sources are also part of the The Second *XMM-Newton* serendipitous source catalog[8] (Watson et al. 2009). Their detection parameters are in agreement with our estimates, however since our pipeline is optimized for high redshift cluster detection, we detect both systems with slightly higher detection likelihoods.

4. Conclusions

1. We have detected two high redshift systems, XMMU J0302.2-0001 at $z = 1.185$ and XMMU J1532.2-0836 at $z = 1.358$. The objects were X-ray selected in the framework of the *XMM-Newton* Distant Cluster Project.
2. We have obtained and analysed medium deep optical/near-infrared imaging and deep optical spectroscopy with VLT/FORS2 and measured spectroscopic redshifts for both systems. We have confirmed XMMU J0302.2-0001 as a bona fide galaxy cluster. Among its spectroscopically confirmed members we find several luminous [O II] emitters. These giant galaxies are likely experiencing residual stochastic star formation activity, possibly triggered by galaxy-galaxy interactions and fluctuations in the overall tidal field.
3. Based on the obtained optical/near-infrared imaging we established that XMMU J0302.2-0001 has a well populated red sequence. In fact, XMMU J0302.2-0001 corresponds to one of the most prominent overdensities of red galaxies ($1.45 < z - H \leq 2.15$) among the known X-ray selected $z > 1$ clusters. Given the currently limited depth of the data for XMMU J1532.2-0836, we can see the bright end of the red sequence (finding two spectroscopical members to have colors consistent with a SSP spectro-photometric sequence for the cluster redshift), but deeper observations will be required to study the galaxy population of the cluster in more detail.
4. From archival *XMM-Newton* data we have estimated the basic physical parameters of XMMU J0302.2-0001. Within the r_{500} aperture we measured the luminosity (0.5−2 keV band) of cluster to be $L_{500} = (8.35 \pm 0.93) \times 10^{43}$ erg s^{-1}. Assuming a self-similar evolution of the $L - M$ scaling relation this value correspond to $M_{500} = (1.2 \pm 0.2) \times 10^{14}\ M_{\odot}$. This ranks XMMU J0302.2-0001 among intermediate mass clusters at its redshift.
5. We confirm the presence of a dynamically bound galaxy system with three concordant redshifts and coincident with XMMU J0302.2-0001. We also find [O II], [Ne III] and [Ne V] emission lines in the optical spectrum of one of the member galaxies making it a likely obscured AGN candidate.
6. We carried out an in-depth X-ray analysis of XMMU J1532.2-0836, showing that its original tentative detection as an extended source can not be confirmed by currently available data. While the nature of the X-ray emission as originating from faint ICM emission can not be ruled out, we conclude that it is likely that the emission is dominated (or possibly even fully caused) by the central AGN. Notwithstanding this, we estimate upper limits on the X-ray properties for the case that the AGN emission is negligible. We estimate the upper limit for the 0.5−2 keV band luminosity to be $L_{500} = (3.81 \pm 1.21) \times 10^{43}$ erg s^{-1} and the corresponding mass $M_{500} = (0.7 \pm 0.2) \times 10^{14}\ M_{\odot}$.
7. We have discussed the effect of non-self similar evolution of the scaling relations on our mass estimates. We find that a no-evolution scenario yields up to 30% higher masses and ∼25% higher temperatures at these redshifts. This strongly underscores the importance of the efforts to properly calibrate these relationships in the redshift regime $z \gtrsim 0.8$.
8. We detected and analysed a third cluster, XMMU J0302.1-0000, which was serendipitously detected together with cluster XMMU J0302.2-0001. This cluster is established to be an intermediate mass system at an intermediate redshift, $z = 0.647$.

We are experiencing a time period when many crucial questions about the cluster population and its evolution can start to be addressed by analysing cluster samples at high redshifts. This is also the objective of the XDCP project, with the main aim to address the evolution of scaling relations and obtain cosmological constraints. The present paper extends the XDCP sample and provides the first analysis of the clusters in preparation for planned deeper studies based on additional optical/near-infrared data. XMMU J1532.2-0836 is scheduled for deep J and Ks imaging by the Hawk-I instrument on the VLT. A *Chandra* observation to investigate the nature of the X-ray emission from this system has also been allocated. For XMMU J0302.2-0001, K band imaging has already been obtained by the Large Binocular Telescope. A joint, multi-wavelength analysis of these (and other XDCP) targets will be discussed in up-coming studies.

Acknowledgements. We acknowledge the support provided by the VLT staff in carrying out the service observations. This work was supported by the DFG under grants Schw536/24-1, Schw 536/24-2, BO 702/16- 3, and the German DLR under grant 50 QR 0802. R.S. acknowledges support by the DFG in the program SPP1177. H.B. acknowledges support for the research group through The Cluster of Excellence "Origin and Structure of the Universe", funded by the Excellence Initiative of the Federal Government of Germany, EXC project number 153. D.P. acknowledges the kind hospitality of the Max-Planck-Institute for extraterrestrial Physik. H.Q. thanks the FONDAP Centro de Astrofisica for partial support. The *XMM-Newton* project is an ESA Science Mission with instruments and contributions directly funded by ESA Member States and the USA (NASA). This research has made use of the NASA/IPAC Extragalactic Database (NED) which is operated by the Jet Propulsion Laboratory, California Institute of Technology, under contract with the National Aeronautics and Space Administration. We thank Andreas Reichert for providing his cluster compilation catalog. We are thankful to Rosario Gonzales-Riestra, Marcella Brusa, Mara Salvato and Angela Bongiorno for useful discussions. We thank the anonymous referee for a fast reply and helpful suggestions.

Appendix A: XMMU J0302.1-0000

The cluster XMMU J0302.1-0000 was detected in the observation OBSID: 0041170102 only ∼2′ from XMMU J0302.2-0001 at an off-axis angle of 11′, with a high confidence extent significance (∼10σ).

We measured the redshift of the cluster ($z = 0.647 \pm 0.003$) from the same VLT/FORS2 data taken for XMMU J0302.2-0001. The redshift is based on the Milvang-Jensen et al. (2008) criterion (Sect. 2.2.2), identifying 8 cluster members (black hashed peak in Fig. 3, bottom left).

[8] amwdb.u-strasbg.fr/2xmmidr3/catentries

This redshift places the cluster below the formal XDCP distant cluster sample limit ($z \geq 0.8$). The galaxy distribution of the cluster well matches the X-ray surface brightness distribution (see Fig. A.1), with the BCG close to the X-ray peak.

We carry out the X-ray analysis as delineated in Sects. 2.1 and 2.3. In a 1′ aperture we detect 140 source counts in PN and 114 in MOS. The estimated beta model core radius is r_C = 30.9″. The growth curves are displayed in Fig. A.4. Both PN and MOS curves are in good agreement and have well established plateau levels with $F_{plat} = (19.83 \pm 2.16) \times 10^{-15}$ erg cm^{-2} s^{-1}.

We estimate the cluster's mass to be $M_{500} = (1.0 \pm 0.2) \times 10^{14}\ M_\odot$ from its measured luminosity $L_{500} = (3.26 \pm 0.33) \times 10^{43}$ erg s^{-1} (0.5–2 keV). This corresponds to a 2.3 keV temperature. The effect of the evolution uncertainty described in Sect. 3.1 is slightly smaller than for the $z > 1$ cases – the no-evolution scenario yields a ∼20% higher M_{500} and ∼13% higher temperature. The physical parameters are summarized in Table A.1.

In Fig. A.1 we display the pseudo-color image of XMMU J0302.1-0000 and in Fig. A.2. The individual frames and photometry are the same as for XMMU J0302.2-0001 and described in Sect. 2.2.2.

The CMD can be found in Fig. A.2. The cluster has a rich red sequence with a BCG coincident with the X-ray centroid. Although the BCG seems to experience a merging activity, its color is in agreement with the SSP model prediction for the cluster redshift (red dashed line in Fig. A.2).

We have obtained spectroscopy also for the very bright X-ray AGN ∼75″ from the cluster center (see Fig. A.3) and find that its redshift is concordant with XMMU J0302.1-0000. At the cluster redshift this is equivalent to ∼0.5 Mpc, i.e. the AGN is associated with the cluster. This source is also contained in the SDSS catalog (Schneider et al. 2007) (quasar SDSS J030206.76-000121.3 at redshift $z = 0.641$).

Similarly to XMMU J0302.2-0001, the cluster XMMU J0302.1-0000 is also part of the BLOX survey catalog (see Sect. 3.4 and Dietrich et al. 2007), detected independently in the X-ray data and through an optical matched filter cluster finder (object ID: BLOX J0302.0-0000.0). The estimated X-ray extent of $r_C = 27.8'' \pm 1.9''$ is fully consistent with our value. The 0.5–2 keV flux estimated by the BLOX survey is $F_X = (29.4 \pm 2.6) \times 10^{-15}$ erg cm^{-2} s^{-1}, i.e. significantly higher than our value. We note however, that their estimate is based on the direct output of the detection pipeline, whereas ours is from a dedicated growth curve analysis which includes several improvements: 1) a visual screening and manual adjustment of masks for contaminating sources (indeed there is a bright point source detected only 20″ from the cluster's core); 2) the redshift and temperature dependence of the energy conversion factor (which is needed to convert the detected counts to flux) is implemented in an iterative fashion and 3) we use the proper response file calculated locally for the clusters position. Finally, the largest part of the difference comes from the fact that the Dietrich et al. (2007) flux is extrapolated to infinity (assuming a beta-model), while our estimate corresponds to a (finite) aperture and is model independent. For a cluster with a large core radius (∼31″), there is a comparatively larger fraction of the total flux (extrapolated to infinity) outside r_{500} than for a cluster with smaller core radius (such as XMMU J0302.2-0001 ($r_C = 14''$), where the agreement with the BLOX survey value is much better).

The BLOX survey significantly underestimates the cluster redshift (their value is 0.4). They estimate a cluster richness of $\lambda_{CL} = 65.9$, where λ_{CL} is the equivalent number of L^* galaxies with the same total optical luminosity as the cluster galaxies (for the exact definition see Postman et al. 1996).

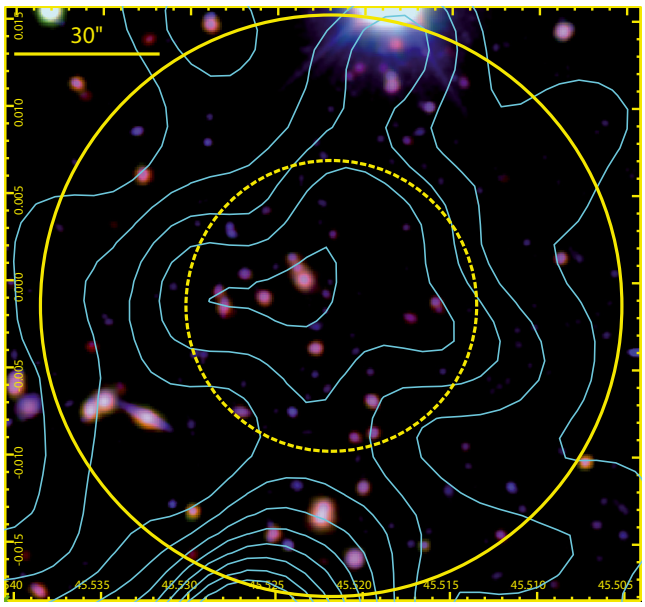

Fig. A.1. Pseudo-color image of the clusters XMMU J0302.1-0000 (*left*, red channel: *H* band, green: *z*, blue: *R*). Adaptively smoothed X-ray contours are overlaid in cyan. Solid/dashed circles mark a 60″/30″ radius region centered on the X-ray detection.

Table A.1. Basic X-ray parameters of XMMU J0302.1-0000. See Table 4 for explanations.

Parameter		Units
α (J2000)[a]	$03^h02^m05.3^s$	
δ (J2000)[a]	−00°00′05.0″	
redshift	0.647 ± 0.003	
$E(z)$	1.43	
Ang. scale	6.92	kpc s^{-1}
n_H[b]	7.05	10^{20} cm^{-2}
$L-M$, $L-T$ self-similar evol.		
F_{500} [0.5–2.0 keV]	19.20 ± 1.95	10^{-15} erg cm^{-2} s^{-1}
L_{500} [0.5–2.0 keV]	3.26 ± 0.33	10^{43} erg s^{-1}
F_{500} [bolometric]	22.78 ± 4.33	10^{-15} erg cm^{-2} s^{-1}
L_{500} [bolometric]	7.71 ± 0.78	10^{43} erg s^{-1}
T_{500}	2.3 ± 0.7	keV
M_{500}	1.0 ± 0.2	$10^{14}\ M_\odot$
r_{500}	0.56	Mpc/arcsec
M_{200}	1.4 ± 0.3	$10^{14}\ M_\odot$
$L-M$, $L-T$ no evol.		
F_{500} [0.5–2.0 keV]	18.88 ± 2.01	10^{-15} erg cm^{-2} s^{-1}
L_{500} [0.5–2.0 keV]	3.14 ± 0.33	10^{43} erg s^{-1}
F_{500} [bolometric]	21.19 ± 4.56	10^{-15} erg cm^{-2} s^{-1}
L_{500} [bolometric]	7.73 ± 0.82	10^{43} erg s^{-1}
T_{500}	2.6 ± 0.6	keV
M_{500}	1.2 ± 0.3	$10^{14}\ M_\odot$
r_{500}	0.59	Mpc
M_{200}	1.7 ± 0.4	$10^{14}\ M_\odot$

Notes. [(a)] X-ray coordinates based on a maximum-likelihood fit of a PSF-folded beta model to the surface brightness distribution; [(b)] values from the LAB HI survey (Kalberla et al. 2005).

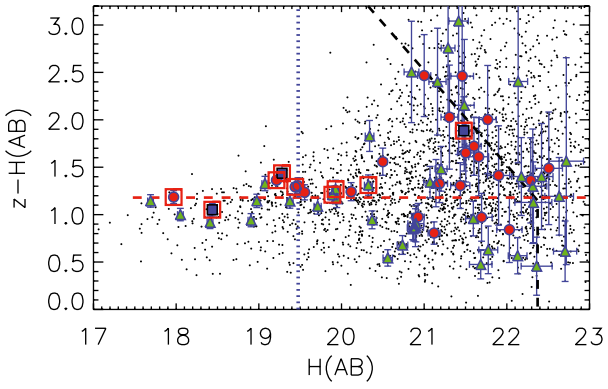

Fig. A.2. The $z - H$ vs. H color−magnitude diagram of the XMMU J0302.1-0000 cluster's field. Red boxes mark secure spectroscopic cluster members. Galaxies with projected cluster centric distance less than 30″ are shown as red circles, with distances between 30″−60″ as green triangles. Galaxies with concordant redshift at >60″ distances have blue squares. The dashed black line marks the 50% completeness limit. The apparent H band magnitude of an L^* galaxy at cluster redshift ($z = 0.647$) is shown with a vertical blue dotted line. We overplot the $z - H$ color of a solar metallicity SSP model with formation redshift $z_f = 5$ and age ~6.3 Gyr (corresponding to the cluster redshift) as a reference (horizontal red dashed line). The presence of a red sequence with analogous colors is evident.

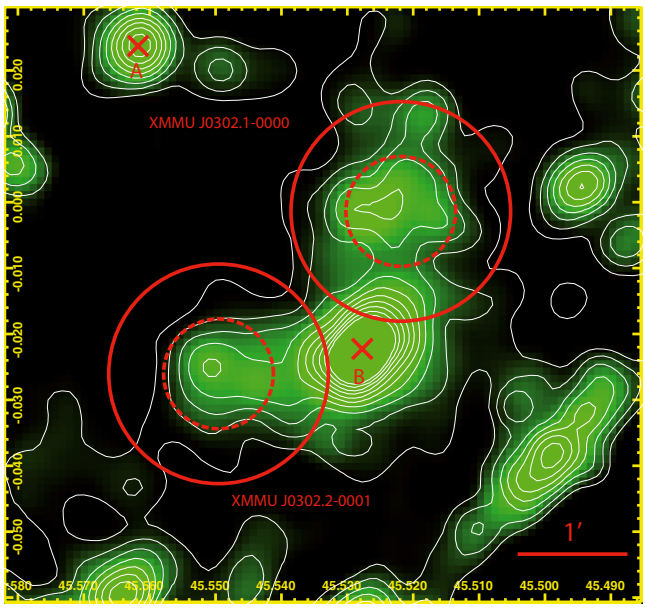

Fig. A.3. Adaptively smoothed 0.5−2 keV X-ray image of the wider neighborhood of XMMU J0302.2-0001 and XMMU J0302.1-0000. The red circles have 60″ radii, while the dashed circles 30″. X-ray contours are overlaid in white. Point A marks the AGN at the redshift of XMMU J0302.2-0001 (SDSS J030214.82+000125.3) and point B the very X-ray bright AGN SDSS J030206.76-000121.3, that has a concordant redshift with the cluster XMMU J0302.1-0000.

The cluster is also part of the second *XMM-Newton* serendipitous source catalog (Watson et al. 2009). The source parameters in this catalog are in good agreement with our values.

In the NED database we find within a 4′ query radius four galaxies with photometric redshifts in agreement with the cluster redshift (i.e. in the range 0.6−0.7) from Waskett et al. (2004). This includes the already mentioned SDSS J030206.76-000121.3.

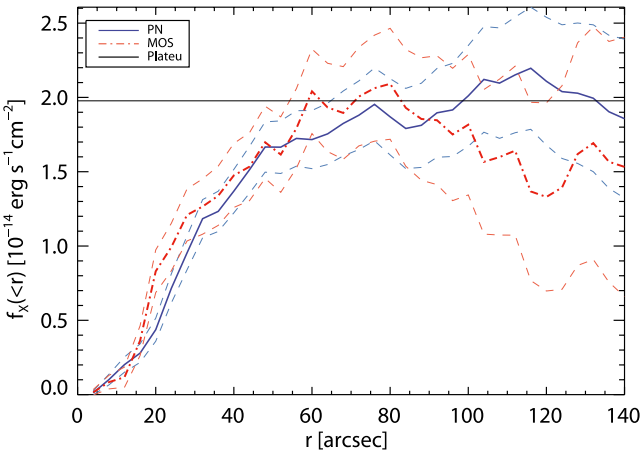

Fig. A.4. Growth curve analysis of XMMU J0302.1-0000. The curves show the encircled cumulative flux as a function of radius (PN: blue curve, combined MOS: red, dot-dashed). Dashed line marks the flux measurement error bars which include the Poisson noise and an additional 5% systematic error from the background estimation. The horizontal line marks the plateau level.

In summary, XMMU J0302.1-0000 is confirmed as an intermediate mass system at intermediate redshift. While it is below the redshift threshold of the XDCP distant cluster sample, owing to its proximity to XMMU J0302.2-0001 it will benefit from upcoming deeper multi-wavelength follow-up data and will be thus an interesting object in its own right.

Appendix B: High redshift cluster detections in the past decade

We have argued in Sect. 1, that in the recent years much important progress has been made in the gradual construction of statistically large, high redshift cluster samples. These samples will allow us to calibrate the scaling relations to redshift ≈1 and beyond and constrain evolutionary models for the ICM and the clusters' galaxy populations.

Reichert et al. (2011) compiled a list of known clusters published up to year 2010 (including), which have secure spectroscopic redshifts and an X-ray luminosity measurement. We select from this catalog a high redshift subsample based on the XDCP project's criterion, i.e. clusters with redshifts $z > 0.8$. While the aim of this catalog is to compile clusters from larger samples, care was taken to include also individually reported high redshift objects. The catalog utilises the latest analysis of each cluster if several are available and therefore whenever it is possible we replace this reference with the year of first *spectroscopic redshift measurement* (understood here as the discovery year). We aim here just for a simple qualitative analysis and therefore these minor effects do not influence our conclusions. The cumulative histogram of the compiled catalog of $z > 0.8$ clusters is shown in Fig. B.1. As we can see the progress made in the past decade (2001−2010) is truly impressive. The total number of clusters given our criteria is 52. Only six of these clusters were known before the year 2001.

In the bottom panel of Fig. B.1 we check whether the total number of clusters grows linearly with time (green dashed line). While the fit is acceptable, there is an indication that the last few years the detection rate has been even larger. An exponential

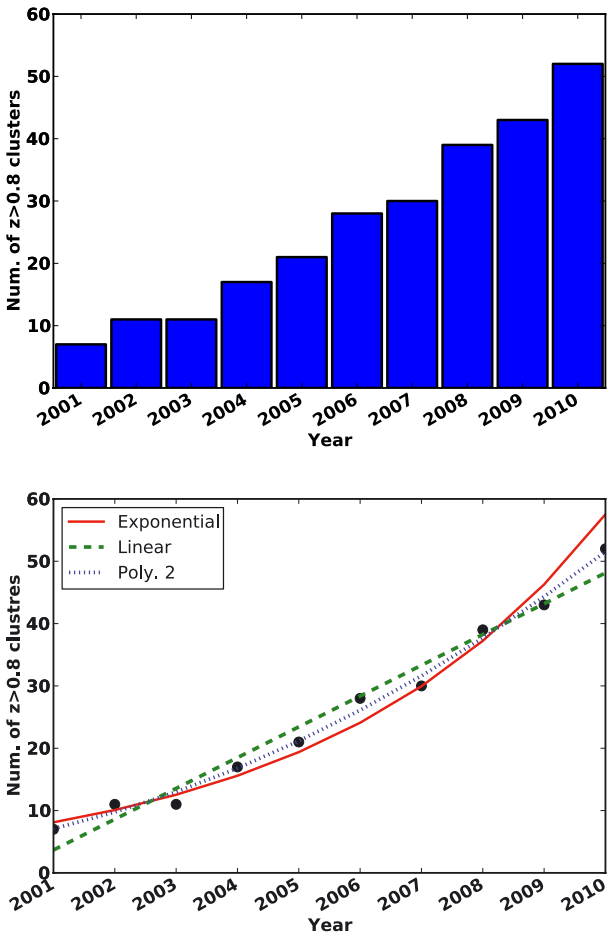

Fig. B.1. *Top*: cumulative histogram of the known clusters with spectroscopic redshift >0.8 and an X-ray luminosity measurement compiled by Reichert et al. (2011). *Bottom*: linear (green dashed line), exponential (red full line) and second order polynomial (blue dotted line) fits to the data in *the top panel*. See the text for discussion.

relation[9] yields an equally good fit (in the sense of the R^2 statistic). An exponential growth might be also preferred if we relax the criteria and would include also clusters with only photometric redshift estimates and not having X-ray luminosity measurements. Especially the Sunyaev-Zel'dovich surveys are currently (e.g. since 2009) the main purveyors of cluster samples with high median redshifts (e.g. ~0.6 from the South Pole Telescope survey, Vanderlinde et al. 2010). We also overplot a second order polynomial in Fig. B.1 (blue dotted line) which well describes the observed detection counts (and confirms the preference for accelerating detection rates). The prediction of this model is 59 clusters given our selection criteria by the end of year 2011.

Upcoming large area X-ray surveys (with *XMM-Newton* and eventually *eRosita*) along with other cluster selection approaches (SZE, optical) and the new near-infrared spectrographs will enable us to further increase our high-z cluster samples. Independently of the exact shape of the growth of our cluster catalogs, the future of high redshift cluster studies certainly seems very promising.

[9] An exponential growth is motivated as a potential instance of Moore's law. A similar growth is observed not only in improvement of computing hardware (and other digital electronic devices), but given a suitable figure-of-merit also in several scientific subfields, e.g. the total number of particles in cosmological N-body simulations or the number of DNA base pairs sequenced per year.

References

Akritas, M. G., & Bershady, M. A. 1996, ApJ, 470, 706
Andreon, S., Maughan, B., Trinchieri, G., & Kurk, J. 2009, A&A, 507, 147
Antonucci, R. R. J., & Miller, J. S. 1985, ApJ, 297, 621
Arnaud, M., Pointecouteau, E., & Pratt, G. W. 2005, A&A, 441, 893
Bailer-Jones, C. A., Bizenberger, P., & Storz, C. 2000, in SPIE Conf. Ser. 4008, ed. M. Iye, & A. F. Moorwood, 1305
Bertin, E., & Arnouts, S. 1996, A&AS, 117, 393
Bielby, R. M., Finoguenov, A., Tanaka, M., et al. 2010, A&A, 523, A66
Böhringer, H., Voges, W., Huchra, J. P., et al. 2000, ApJS, 129, 435
Bullock, J. S., Kolatt, T. S., Sigad, Y., et al. 2001, MNRAS, 321, 559
Cooper, M. C., Newman, J. A., Weiner, B. J., et al. 2008, MNRAS, 383, 1058
Cristiani, S., Trentini, S., La Franca, F., et al. 1996, A&A, 306, 395
De Luca, A., & Molendi, S. 2004, A&A, 419, 837
Dietrich, J. P., Erben, T., Lamer, G., et al. 2007, A&A, 470, 821
Elbaz, D., Daddi, E., Le Borgne, D., et al. 2007, A&A, 468, 33
Fakhouri, O., Ma, C., & Boylan-Kolchin, M. 2010, MNRAS, 406, 2267
Fassbender, R. 2008, Ph.D. thesis [arXiv:0806.0861]
Fassbender, R., Böhringer, H., Santos, J. S., et al. 2011a, A&A, 527, A78
Fassbender, R., Nastasi, A., Böhringer, H., et al. 2011b, A&A, 527, L10
Finn, R. A., Desai, V., Rudnick, G., et al. 2010, ApJ, 720, 87
Finoguenov, A., Watson, M. G., Tanaka, M., et al. 2010, MNRAS, 403, 2063
Garilli, B., Fumana, M., Franzetti, P., et al. 2010, PASP, 122, 827
Gerke, B. F., Newman, J. A., Faber, S. M., et al. 2007, MNRAS, 376, 1425
Giocoli, C., Moreno, J., Sheth, R. K., & Tormen, G. 2007, MNRAS, 376, 977
Gladders, M. D., & Yee, H. K. C. 2005, ApJS, 157, 1
Gobat, R., Daddi, E., Onodera, M., et al. 2011, A&A, 526, A133
Groves, B. A., Heckman, T. M., & Kauffmann, G. 2006, MNRAS, 371, 1559
Hayashi, M., Kodama, T., Koyama, Y., et al. 2010, MNRAS, 402, 1980
Henry, J. P., Salvato, M., Finoguenov, A., et al. 2010, ApJ, 725, 615
Hilton, M., Lloyd-Davies, E., Stanford, S. A., et al. 2010, ApJ, 718, 133
Hu, W., & Kravtsov, A. V. 2003, ApJ, 584, 702
Kaiser, N. 1986, MNRAS, 222, 323
Kalberla, P. M. W., Burton, W. B., Hartmann, D., et al. 2005, A&A, 440, 775
Kuntz, K. D., & Snowden, S. L. 2008, A&A, 478, 575
Kurtz, M. J., & Mink, D. J. 1998, PASP, 110, 934
Lidman, C., Rosati, P., Tanaka, M., et al. 2008, A&A, 489, 981
Marriage, T. A., Acquaviva, V., Ade, P. A. R., et al. 2011, ApJ, submitted [arXiv:1010.1065]
Martig, M., & Bournaud, F. 2008, MNRAS, 385, L38
Milvang-Jensen, B., Noll, S., Halliday, C., et al. 2008, A&A, 482, 419
Mullis, C. R., Rosati, P., Lamer, G., et al. 2005, ApJ, 623, L85
Navarro, J. F., Frenk, C. S., & White, S. D. M. 1997, ApJ, 490, 493
Pacaud, F., Pierre, M., Adami, C., et al. 2007, MNRAS, 382, 1289
Papovich, C., Momcheva, I., Willmer, C. N. A., et al. 2010, ApJ, 716, 1503
Pierini et al. 2011, submitted
Planck Collaboration, Ade, P. A. R., Aghanim, N., et al. 2011, A&A, submitted [arXiv:1101.2024]
Postman, M., Lubin, L. M., Gunn, J. E., et al. 1996, AJ, 111, 615
Pratt, G. W., Croston, J. H., Arnaud, M., & Böhringer, H. 2009, A&A, 498, 361
Reichert et al. 2011, submitted
Schneider, D. P., Hall, P. B., Richards, G. T., et al. 2007, AJ, 134, 102
Schwope, A. D., Lamer, G., de Hoon, A., et al. 2010, A&A, 513, L10
Scodeggio, M., Franzetti, P., Garilli, B., et al. 2005, PASP, 117, 1284
Stanek, R., Rasia, E., Evrard, A. E., Pearce, F., & Gazzola, L. 2010, ApJ, 715, 1508
Stanford, S. A., Eisenhardt, P. R., Brodwin, M., et al. 2005, ApJ, 634, L129
Stanford, S. A., Romer, A. K., Sabirli, K., et al. 2006, ApJ, 646, L13
Šuhada, R., Song, J., Böhringer, H., et al. 2010, A&A, 514, L3
Tanaka, M., Finoguenov, A., & Ueda, Y. 2010, ApJ, 716, L152
Vanderlinde, K., Crawford, T. M., de Haan, T., et al. 2010, ApJ, 722, 1180
Véron-Cetty, M., & Véron, P. 2006, A&A, 455, 773
Vikhlinin, A., Burenin, R. A., Ebeling, H., et al. 2009, ApJ, 692, 1033
Waskett, T. J., Eales, S. A., Gear, W. K., et al. 2004, MNRAS, 350, 785
Watson, M. G., Schröder, A. C., Fyfe, D., et al. 2009, A&A, 493, 339
Williamson, R., Benson, B. A., High, F. W., et al. 2011 [arXiv:1101.1290]